Preprint of the manuscript submitted to Mechanical System and Signal Processing on Sept 26, 2025. The final published version is available at https://doi.org/10.1016/j.ymssp.2026.113965 (Mechanical Systems and Signal Processing 247:113965, 2026).

A physics-augmented deep learning framework for structural dynamic load identification with FRF-guided state expansion

Xinhao An [a], Jilin Hou [a,*], Łukasz Jankowski [b], Qingxia Zhang [c]

[a] Department of Civil Engineering, Dalian University of Technology, 116023 Dalian, China;
[b] Institute of Fundamental Technological Research, Polish Academy of Sciences, 02-106 Warsaw, Poland;
[c] School of Civil Engineering, Dalian Minzu University, 116600 Dalian, China

Abstracts:

Structural load identification is a critical technique that facilitates safety monitoring and performance assessment of engineering structures, activities that hold significant engineering importance. Current mainstream methods face two major challenges: traditional physical model inversion techniques require precise knowledge of structural parameters and thus are highly sensitive to modeling errors, while purely data-driven approaches based deep learning offer powerful nonlinear mapping capabilities but lack integration with physical laws and rely heavily on large volumes of labeled data. To address these issues, this paper proposes a physics-augmented deep learning (PADL) framework for structural dynamic load identification. First, based on the measured dynamic response of the structure and a simplified structural model, an initial load estimate is obtained through the frequency response function (FRF) inversion technique. Additionally, frequency-domain relationships between different types of responses are exploited to approximately reconstruct unmeasured responses, which further augments available information under the constraints of physical laws. Notably, the physical model employed in this process does not require precise structural parameters: even a simplified, inaccurate model is sufficient to provide the necessary physical constraints. Next, the augmented data is fed into a lightweight LSTM network for residual error compensation, with the output layer designed as a linear mapping without an activation function. This design overcomes the limitation of output boundedness, enabling load extrapolation beyond the extreme values of the training data through an explicit scaling mechanism in the weight matrix. Finally, numerical simulations and laboratory tests are performed to demonstrate the effectiveness of the proposed PADL framework in identification of structural dynamic loads.

Keyword: Load identification; Deep learning; Hybrid modeling; Physics-augmented; Small training samples; Structural health monitoring

* Corresponding author.
E-mail address: houjilin@dlut.edu.cn (JL. Hou)

1. Introduction

Structural load identification [1–3] is one of the core research directions in engineering mechanics and intelligent monitoring, where its main aim is to estimate the temporal and spatial distribution of load characteristics. It has significant practical engineering value in structural health assessment, damage diagnosis, and service life prediction, and has attracted extensive attention in fields such as automotive [4], aerospace [5], and civil engineering [6].

The task of load identification based on measured responses is essentially a dynamic inverse problem, where the goal is to infer unknown external loads from known structural responses. Current mainstream load identification methods can be divided into three categories: analytical methods based on physical models, purely data-driven machine learning methods, and physics-data hybrid modeling methods.

Physical model-based methods rely on the mathematical inversion of the governing equations of structural dynamics and can be categorized into time-domain and frequency-domain approaches. Time-domain load identification methods most commonly employ Kalman filtering, which is based on a state-space modeling framework and enables dynamic estimation of system state and external loads through a recursive algorithm [7–9]. This approach can also be extended to nonlinear systems by using unscented or extended Kalman filters (UKF, EKF) [10,11]. Alternatively, an observation equation can be constructed using the time-domain convolution of the system impulse response function with the unknown loads. The resulting equation is ill-conditioned and is typically solved with regularization techniques to obtain numerically stable load identification results [12]. Frequency-domain methods utilize the linear load–response relationship in the frequency domain. By constructing the frequency response function (FRF) and performing the inverse operation separately at each frequency line, the external excitation can be identified directly from the response signal. Alqam et al [13] used the strain frequency response function (SFRF) and the displacement frequency response function (DFRF) for indirect load identification. Jia et al. [14] constructed the FRF based on modal parameters; random dynamic loads were then identified using a weighted regularization method based on proper orthogonal decomposition (POD), which reduced the ill-conditioning of inverse operations in the frequency domain of the classical least squares generalized method.

With the development of machine learning, purely data-driven deep learning methods have been developed that discard physical model constraints and directly construct end-to-end deep neural network mapping from responses to loads [15]. Convolutional neural network (CNN) is a widely used deep learning architecture, which efficiently extracts spatial and spatio-temporal correlation features from signals by means of local receptive fields and weight-sharing mechanisms. For example, Yang et al. [16] proposed a dynamic load identification method based on a depth-expansive convolutional neural

network (DCNN). He et al. [17,18] developed a one-dimensional convolutional neural network (1D-CNN) model with an attention mechanism for identifying stochastic dynamic loads of aircraft. Recurrent neural networks (RNNs) and their derived models show unique advantages in time-dependent modeling. Yang et al. [19] used an RNN to identify sinusoidal, impulsive, and stochastic loads of simply supported beams. To address the gradient explosion and vanishing problems inherent in RNN networks, Hochreiter and Schmidhuber [20] proposed the long short-term memory (LSTM) network, which stabilizes gradient transfer through a gating mechanism and provides robust temporal modeling. Zhou et al. [21] used LSTM for impact load identification in nonlinear structures. With increasing demand for computational efficiency, the gated recurrent unit (GRU) [22], a lightweight variant of LSTM, has gradually gained attention in dynamic load identification [23]. Moreover, hybrid neural architectures that fuse different modules have also been applied [24]. Although data-driven methods show strong feature representation ability in complex systems, their "black-box" nature leads to insufficient interpretability and a heavy dependence on massive training data.

In recent years, to address the "black-box" nature of purely data-driven methods, efforts have been made to integrate the advantages of physical models with data-driven approaches to enhance the interpretability and effectiveness of neural networks. One approach is to introduce physical constraints into the neural model to construct physics-constrained neural networks [25,26]. For instance, Moradi et al. [27] proposed a new physics-informed neural network (PINN) architecture for identifying structural input loads by embedding discretized partial differential equations into the deep learning framework. Zhou et al. [28] achieved dynamic load identification with small training samples by incorporating a physics-based loss term into the loss function as a physical constraint. Liu et al. [29] developed a hybrid physics and data-driven approach by embedding the structural impulse response function as a non-trainable layer in the neural network to identify moving loads. However, the added physics-driven loss term imposes limitations on the applicability of this approach, such as restricting it to linear systems or affecting its performance due to errors in the assumed physical model. Another approach is to chain physical methods with data-driven methods, where neural networks compensate for the identification errors caused by inaccurate physical models. Yin et al. [30] proposed the APHYNITY framework, which uses data-driven models to enhance the incomplete physical dynamics described by differential equations. Ji et al. [31] used neural networks to map the residuals between Kalman filter estimates and the true loads. These methods avoid the instability caused by directly embedding physical models into the loss function and show significant application potential, although they still require considerable amounts of training data.

To address the above challenges, this paper proposes a Physics-Augmented Deep Learning (PADL) framework for dynamic load identification. First, a rough estimate of the load and the full-state response is obtained using an approximate reduced-order physical model. Subsequently, a lightweight neural

network is employed to compensate for the residual errors introduced by the simplified model. The proposed method enhances physical interpretability and reduces dependence on large amounts of training data. Moreover, it is sensor-agnostic and enables load identification with heterogeneous sensor types. The key innovation lies in the state extension of the physical model, which provides the neural network with rich, physically consistent prior data. This allows the network to learn the low-dimensional residual mapping directly, instead of fitting complex dynamics in high-dimensional space.

This paper is organized as follows. Section 2 introduces the PADL framework and its components. Section 3 presents the load identification performance of PADL in numerical simulations. Section 4 demonstrates the effectiveness of PADL in identifying random and impulsive loads through laboratory experiments.

2. PADL framework

The proposed PADL framework consists of two elements: an initial model-based and approximate load estimation and state reconstruction (Section 2.1), and a subsequent LSTM-based lightweight neural correction module (Section 2.2). These components are integrated to form the PADL framework, as described in Section 2.3.

2.1 FRF-based load estimation and full-state reconstruction

For a linear structure under forced vibration, the governing equation of motion is expressed as:

$$\boldsymbol{M}\ddot{\boldsymbol{u}}(t) + \boldsymbol{C}\dot{\boldsymbol{u}}(t) + \boldsymbol{K}\boldsymbol{u}(t) = \boldsymbol{N}\boldsymbol{f}(t) \tag{1}$$

where $\boldsymbol{u}(t)$, $\dot{\boldsymbol{u}}(t)$ and $\ddot{\boldsymbol{u}}(t)$ denote the displacement, velocity and acceleration vectors, respectively; $\boldsymbol{M}$, $\boldsymbol{C}$ and $\boldsymbol{K}$ denote the mass, damping, and stiffness matrices, respectively; $\boldsymbol{f}(t)$ is the vector of external excitation forces; and $\boldsymbol{N}$ is the force distribution matrix. Applying the Fourier transform to Eq.(1), the frequency-domain equation of motion becomes:

$$-\omega^2\boldsymbol{M}\boldsymbol{U}(\omega) + \omega j\boldsymbol{C}\boldsymbol{U}(\omega) + \boldsymbol{K}\boldsymbol{U}(\omega) = \boldsymbol{N}\boldsymbol{F}(\omega) \tag{2}$$

where $\boldsymbol{U}(\omega)$ and $\boldsymbol{F}(\omega)$ denote the frequency-domain displacement response vector and excitation force vector, respectively. Rearranging Eq.(2), the displacement response is derived as:

$$\boldsymbol{U}(\omega) = (-\omega^2\boldsymbol{M} + \omega j\boldsymbol{C} + \boldsymbol{K})^{-1}\boldsymbol{N}\boldsymbol{F}(\omega) = \boldsymbol{H}(\omega)\boldsymbol{F}(\omega) \tag{3}$$

where $\boldsymbol{H}(\omega)$ is the force-to-displacement FRF, which characterizes the linear transformation between the displacement response and the excitation force in the frequency domain.

The full-state vector $\boldsymbol{Z}(\omega)$ in the frequency domain is defined as:

$$\boldsymbol{Z}(\omega) = \begin{bmatrix} \boldsymbol{U}(\omega) \\ \dot{\boldsymbol{U}}(\omega) \\ \ddot{\boldsymbol{U}}(\omega) \end{bmatrix} = \boldsymbol{L}\boldsymbol{U}(\omega) \tag{4}$$

where $\dot{\boldsymbol{U}}(\omega)$ and $\ddot{\boldsymbol{U}}(\omega)$ represent the velocity and acceleration responses in the frequency domain, respectively, and $\boldsymbol{L} = [\boldsymbol{I}, j\omega\boldsymbol{I}, -\omega^2\boldsymbol{I}]^{\mathrm{T}}$, with $\boldsymbol{I}$ being the identity matrix, is the response transformation matrix that maps displacements to all state variables.

Using the observation matrix $\boldsymbol{C_0}$, the observed frequency-domain response is expressed as:

$$\boldsymbol{Y}(\omega) = \boldsymbol{C_0}\boldsymbol{Z}(\omega) \tag{5}$$

According to Eq.(3) ~ Eq.(5), the excitation force spectrum $\boldsymbol{F}(\omega)$ can be estimated as follows:

$$\widetilde{\boldsymbol{F}}(\omega) = (\boldsymbol{C_0}\boldsymbol{L}\boldsymbol{H})^{+}\boldsymbol{Y}(\omega) \tag{6}$$

where $(\cdot)^{+}$ denotes the generalized inverse, computed as $\boldsymbol{X}^{+} = (\boldsymbol{X}^{\mathrm{H}}\boldsymbol{X})^{-1}\boldsymbol{X}^{\mathrm{H}}$, with $(\cdot)^{\mathrm{H}}$ representing the conjugate transpose, and $\boldsymbol{X}$ being an arbitrary matrix. According to Eq.(3) and Eq.(4), the full-state vector $\widetilde{\boldsymbol{Z}}(\omega)$ is reconstructed in the frequency domain as:

$$\widetilde{\boldsymbol{Z}}(\omega) = \boldsymbol{L}\boldsymbol{H}\widetilde{\boldsymbol{F}}(\omega) \tag{7}$$

Finally, the estimates of the excitation force and the full state responses in the time domain are obtained through the inverse Fourier transform:

$$\tilde{\boldsymbol{f}}(t) = \boldsymbol{\mathcal{F}}^{-1}\{\widetilde{\boldsymbol{F}}(\omega)\} \tag{8}$$

$$\tilde{\boldsymbol{z}}(t) = \boldsymbol{\mathcal{F}}^{-1}\{\widetilde{\boldsymbol{Z}}(\omega)\} \tag{9}$$

where $\boldsymbol{\mathcal{F}}^{-1}\{\cdot\}$ denotes the inverse Fourier transform.

The above procedure is fundamentally equivalent to a linear deconvolution process. It requires precise knowledge of the system's physical parameters (mass, damping, stiffness) and is highly sensitive to model inaccuracies. Therefore, initial model correction is crucial, that is, aligning the analytical matrices $\boldsymbol{M}, \boldsymbol{C}$ and $\boldsymbol{K}$ with the true system dynamics. However, the method proposed in this paper requires only a simplified or approximate model to provide constraints that encode physical laws. Effectively, only rough estimates of the load and the full-state response are necessary for the subsequent data-driven component.

Moreover, the FRF-based load estimation and full-state reconstruction procedure is generally agnostic to sensor type due to its unified formulation, as no inherent constraints are imposed on the type of the measured responses. This eliminates dependence on specific response categories and enables load

identification, via the generalized inverse of the FRF matrix, independent of specific sensor configurations. This contrasts with alternative approaches such as the Kalman filter with unknown input (DKF-UI), which requires accelerometers at the excitation locations [32], or the augmented Kalman filter (AKF), which demands displacement responses to address the sparsity of the observation matrix [33]. In summary, the simplicity and consistent formulation of the FRF-based method, which reduces dependence on specific measurement types, are the key reasons it is selected in this study for the physics-informed state expansion.

2.2 LSTM network

The LSTM network is a data-driven sequential modeling technique widely recognized for its ability to capture complex temporal dependencies in a numerically stable manner. In contrast to physics-based models, LSTM networks do not require prior knowledge of system parameters but instead rely on sufficient training data to capture dynamic characteristics. Fig. 1 depicts the internal structure of a single LSTM cell, highlighting its three essential gates (forget, input, and output) as well as the cell state update process. The core components of an LSTM cell include the following steps.

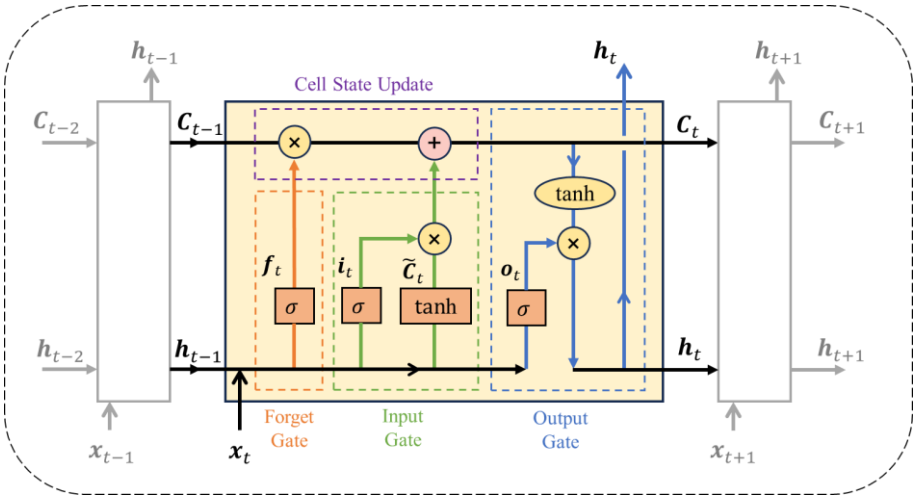

Fig. 1. Schematic representation of an LSTM cell

(1) Forget gate: selective retention of historical information

The forget gate determines the extent to which information from the previous cell state $\boldsymbol{C}_{t-1}$ should be retained, based on the current input $\boldsymbol{x}_t$ and the previous hidden state $\boldsymbol{h}_{t-1}$:

$$\boldsymbol{f}_t = \sigma\left(\boldsymbol{W}_{xf}\boldsymbol{x}_t + \boldsymbol{W}_{hf}\boldsymbol{h}_{t-1} + \boldsymbol{b}_f\right) \tag{10}$$

where $\boldsymbol{W}_{xf}$ and $\boldsymbol{W}_{hf}$ are weight matrices for the input and hidden state, respectively; $\boldsymbol{b}_f$ is the bias vector; $\boldsymbol{\sigma}(\cdot)$ denotes the sigmoid activation function, which maps its argument into the range (0, 1). A value of $\boldsymbol{f}_t \approx 1$ indicates full retention of the cell state component, while $\boldsymbol{f}_t \approx 0$ implies complete

discarding. By controlling memory retention, the forget gate mitigates the accumulation of irrelevant historical information and effectively addresses long-term dependency problems.

(2) Input gate: controlled integration of new information

The input gate governs how much new information from the current input $\boldsymbol{x}_t$ and the previous hidden state $\boldsymbol{h}_{t-1}$ is added to the cell state. It involves two steps with gate activation and candidate cell state generation:

$$\boldsymbol{i}_t = \sigma(\boldsymbol{W}_{xi}\boldsymbol{x}_t + \boldsymbol{W}_{hi}\boldsymbol{h}_{t-1} + \boldsymbol{b}_i) \tag{11}$$

$$\widetilde{\boldsymbol{C}}_t = \tanh(\boldsymbol{W}_{xc}\boldsymbol{x}_t + \boldsymbol{W}_{hc}\boldsymbol{h}_{t-1} + \boldsymbol{b}_c) \tag{12}$$

where $\boldsymbol{W}_{xi}, \boldsymbol{W}_{hi}, \boldsymbol{W}_{xc}, \boldsymbol{W}_{hc}$ are weight matrices; $\boldsymbol{b}_i$ and $\boldsymbol{b}_c$ are bias vectors; $\boldsymbol{i}_t$ is the input gate activation; and $\widetilde{\boldsymbol{C}}_t$ denotes the candidate cell state, scaled by the hyperbolic tangent function $\tanh(\cdot)$ to the range (-1, 1).

(3) Cell state update: memory consolidation

The cell state $\boldsymbol{C}_t$ is updated by combining the retained historical content ($\boldsymbol{f}_t \odot \boldsymbol{C}_{t-1}$) and the filtered new information ($\boldsymbol{i}_t \odot \widehat{\boldsymbol{C}}_t$):

$$\boldsymbol{C}_t = \boldsymbol{f}_t \odot \boldsymbol{C}_{t-1} + \boldsymbol{i}_t \odot \widetilde{\boldsymbol{C}}_t \tag{13}$$

where $\odot$ denotes element-wise multiplication. The forget gate $\boldsymbol{f}_t$ acts as a low-pass filter, preserving low-frequency (long-term) patterns. The input gate $\boldsymbol{i}_t$ functions as a high-pass filter, emphasizing high-frequency (transient) features. The additive update rule facilitates gradient preservation across time and helps to alleviate the vanishing and exploding gradient problems during training.

(4) Output gate: state-dependent hidden state generation

The output gate determines how much of the current cell state $\boldsymbol{C}_t$ is revealed to subsequent layers:

$$\boldsymbol{o}_t = \sigma(\boldsymbol{W}_{xo}\boldsymbol{x}_t + \boldsymbol{W}_{ho}\boldsymbol{h}_{t-1} + \boldsymbol{b}_o) \tag{14}$$

$$\boldsymbol{h}_t = \boldsymbol{o}_t \tanh(\boldsymbol{C}_t) \tag{15}$$

where $\boldsymbol{W}_{xo}$ and $\boldsymbol{W}_{ho}$ are weights matrices; $\boldsymbol{b}_o$ is the bias vector; and $\boldsymbol{o}_t$ determines the parts of the internal state $\boldsymbol{C}_t$ that are exposed as the output $\boldsymbol{h}_t$. The mapping $\tanh(\boldsymbol{C}_t)$ normalizes the values to enhance numerical stability. This design decouples memory storage from contextual exposure, which allows the model to control the information shared externally.

2.3 Components of PADL

The proposed hybrid modeling framework, PADL, is illustrated in Fig. 2. Its architecture integrates physics-based state augmentation with a lightweight data-driven learning module. The overall implementation process can be divided into four key stages:

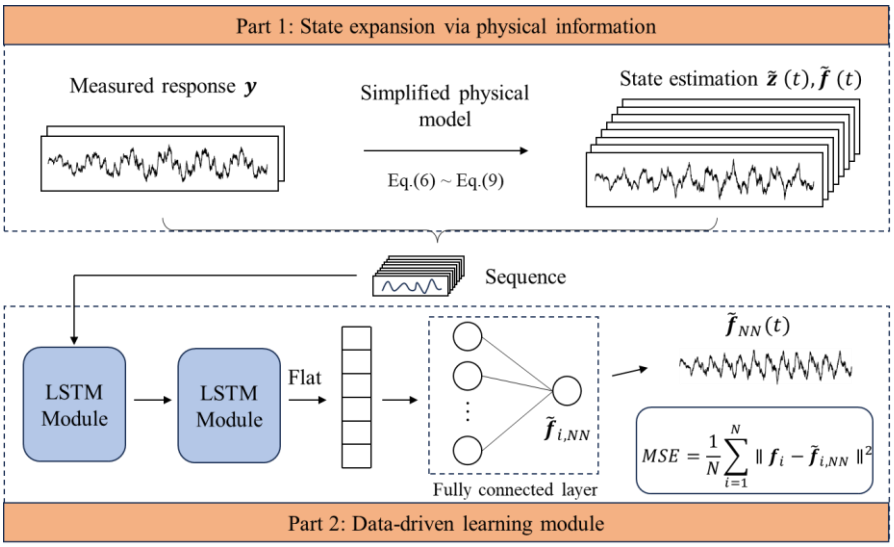

Fig. 2. Flowchart of the PADL framework

(1) Load estimation and state expansion via physical information

The proposed methodology begins with the development of a finite element model of the structure and its FRF function. As the FRF method can be computationally expensive for high-dimensional systems, the model may be simplified and approximate only. The FRF is then employed, using measured responses, to estimate the external force $\tilde{\boldsymbol{f}}(t)$ and the full state vector $\tilde{\boldsymbol{z}}(t)$. Structural physical properties (such as mass, stiffness, and damping matrices) are embedded within the FRF to ensure that the computed estimates are physically consistent. This approach compensates for the sparsity of sensor data: it enriches the feature space with theoretically grounded dynamics that, even if approximate, maintain the physical relationships among system variables. In other words, the FRF-based estimates serve as physically informed priors. They enable the subsequent learning module to exploit correlations between system states and unknown loads, even in the absence of complete measurements.

(2) Data preparation for temporal modeling

The input to the LSTM model consists of three components: the measured system responses $\boldsymbol{y}(t)$, the estimated external force $\tilde{\boldsymbol{f}}(t)$, and the reconstructed unobserved states $\tilde{\boldsymbol{z}}(t)$. These features are segmented using a moving time window into several time-series sequences of length l_{sq}, chosen to capture the characteristic timescales of the system dynamics. Each such sequence is then reshaped into a tensor $\boldsymbol{X} \in \mathbb{R}^{l_{\mathrm{sq}} \times n_{\mathrm{feature}}}$, where n_{feature} represents the number of features per timestep and equals

the total number of sensors, states, and estimated loads. This preprocessing step ensures compatibility with the LSTM architecture and allows it to capture temporal dependencies across both latent (estimated) and observed variables. The feature tensor $\boldsymbol{X}$ thus serves as a hybrid input that combines measurement data and its physics-based extrapolations.

(3) LSTM and fully connected layer architecture

The neural module, designed to learn the mapping between the multi-dimensional input tensor $\boldsymbol{X}$ and the target load, consists of two stacked LSTM layers. The final hidden states produced by the second LSTM layer are flattened into a vector $\boldsymbol{x}_{fc} \in \mathbb{R}^{n_{\text{hidden}}}$ and passed to a fully connected (FC) layer for dimensionality reduction:

$$\tilde{\boldsymbol{f}}_{NN} = \boldsymbol{W}_{fc}\boldsymbol{x}_{fc} + \boldsymbol{b}_{fc} \tag{16}$$

where $\tilde{\boldsymbol{f}}_{NN} \in \mathbb{R}^{n_{\text{output}}}$ denotes the predicted load, while $\boldsymbol{W}_{fc}$ and $\boldsymbol{b}_{fc}$ are the weights and biases of the FC layer.

Notably, the FC layer does not employ a bounded activation function such as sigmoid or tanh, but instead uses a linear output. This design choice ensures that the predicted force values are not constrained by the maximum range of the training data. It enables the model to generalize to force magnitudes beyond those seen during training. The impact of this linear activation strategy is further analyzed in Section 3.

(4) Loss function

The hybrid modeling network is trained using the mean squared error (MSE) loss, defined as:

$$\mathcal{L}_{MSE} = \frac{1}{N}\sum_{i=1}^{N}\left\|\boldsymbol{f}_i - \tilde{\boldsymbol{f}}_{i,NN}\right\|^2 \tag{17}$$

where N is the number of training samples, $\boldsymbol{f}_i$ denotes the ground-truth force, and $\tilde{\boldsymbol{f}}_{i,NN}$ is the network prediction. The MSE loss penalizes deviations between predicted and actual force values at each time step and guides the network toward accurate estimation.

By integrating simplified physics-based modeling with data-driven compensation, the proposed methodology enables load identification without the need for a fully precise physical model or extensive training datasets. The physics-derived FRF framework provides an initial estimation of external load and unmeasured system states (displacements, velocities, accelerations) that serves as a first-principles-informed prior. Then, the lightweight network functions as a corrector by learning the residuals between the FRF-based estimates and the true loads. This approach preserves model interpretability while reducing reliance on exhaustive datasets and precise physical knowledge. It thus offers a practical balance between simplicity and real-world applicability.

3. Numerical simulation

A numerical case of load identification in forced vibration is presented using a two-span frame model to demonstrate the advantages of the proposed PADL method compared to purely data-driven and purely physics-based approaches.

3.1 Finite element model and response simulation

A finite element model (FEM) of a frame structure was created as shown in Fig. 3(a). The story height and span are both 0.4 m. The beams and columns share the same material properties, with an elastic modulus of 2×10^9 Pa, a density of 2×10^3 kg/m³, a section height of 0.01 m, and a section width of 0.15 m. The structure was divided into 80 elements, totaling 216 degrees of freedom. The mass and stiffness matrices were constructed, and the damping matrix was calculated according to the Rayleigh method. The damping ratios for the first two modes were taken as 0.05.

Tapered sine loads at different frequencies were applied to the second story of the structure. A total of 6 trials were simulated, and the loads were sorted by their maximum amplitudes, as shown in Fig. 3 (b). The load frequencies for each trial are shown in Fig. 3(c), and the load time histories are shown in Fig. 3 (d). The structural responses were calculated using the Newmark-β method, and 20% Gaussian white noise was added to the generated responses. The sampling frequency was set to 1000 Hz. As an example, the acceleration responses at observation points on floors 1-4 are shown in Fig. 4 for Trial 4.

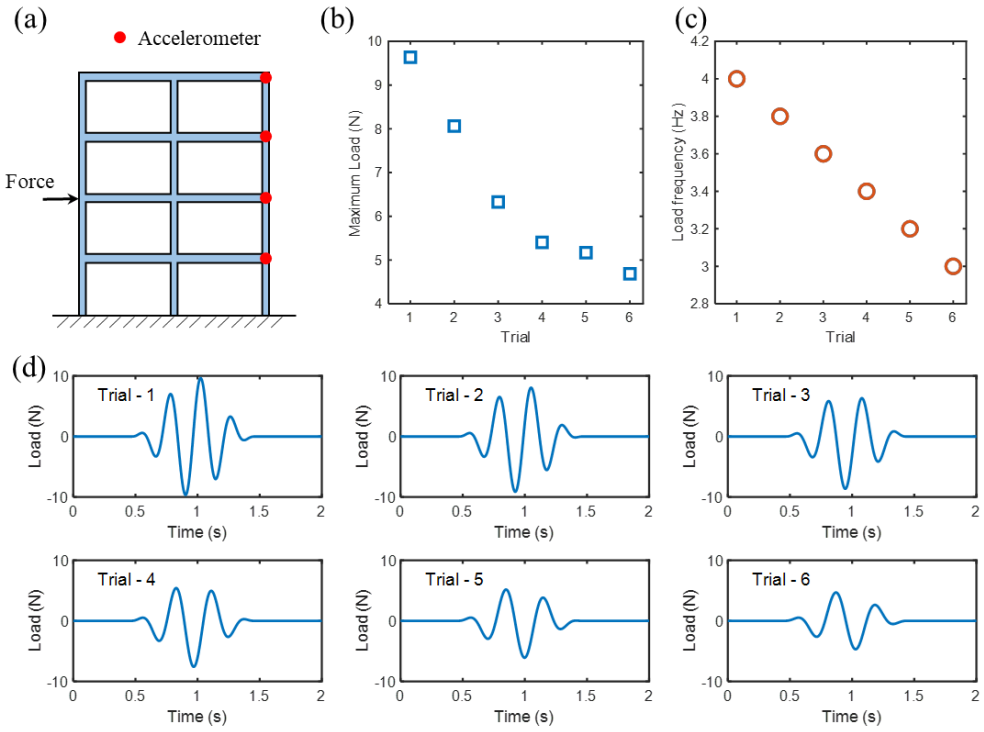

Fig. 3. Structure and load: (a) Frame structure and response measurement points; (b) Maximum load amplitudes; (c) Load frequencies; (d) Load time histories

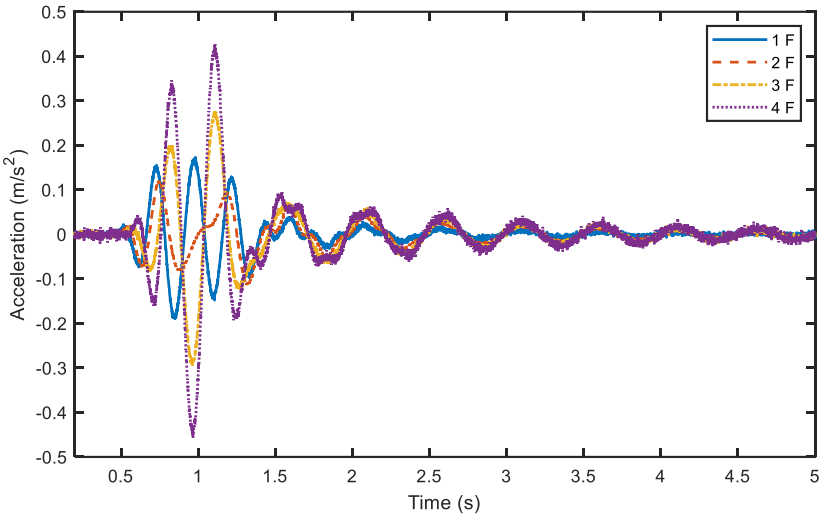

Fig. 4. Acceleration responses of floors 1-4 observed in Trial 4

3.2 Load identification results

In this section, three load identification methods were compared: the PADL method, the pure data-driven method (DL), and the pure physical model method (FEM). The schematic diagrams of these three methods are shown in Fig. 5.

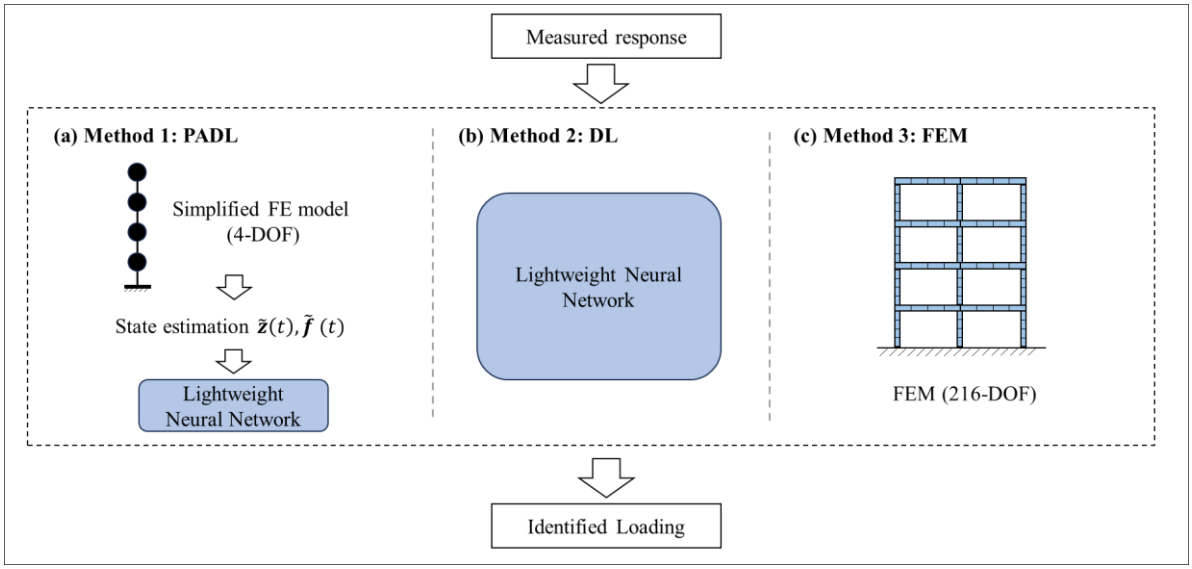

Fig. 5. Three load identification methods

(1) PADL method: A simplified 4-DOF model with inaccurate physical parameters, as shown in Fig. 5(a), was used as the prior information for the structural model. The floor masses, m_1, m_2, m_3, m_4, were set to 10 kg, 20 kg, 30 kg, 40 kg, respectively. The inter-floor stiffness values, k_1, k_2, k_3, k_4, were set to 10 kN/m, 15 kN/m, 20 kN/m, 25 kN/m, respectively. These values were arbitrarily chosen and intentionally varied to create differences in the mass and stiffness of each floor, in order to distinguish

this model from an exact model that has identical stiffness and mass for each floor. The mass and stiffness matrices of the simplified model were constructed as follows:

$$\boldsymbol{M} = \mathrm{diag}([m_1, m_2, m_3, m_4]) \tag{18}$$

$$\boldsymbol{K} = \begin{bmatrix} k_1 + k_2 & -k_2 & 0 & 0 \\ -k_2 & k_2 + k_3 & -k_3 & 0 \\ 0 & -k_3 & k_3 + k_4 & -k_4 \\ 0 & 0 & -k_4 & k_4 \end{bmatrix} \tag{19}$$

Next, the damping matrix was constructed assuming a damping ratio of 0.05. Since the accelerations of floors 1-4 were observed, the observation matrix was defined as follows:

$$\boldsymbol{C}_0 = \begin{bmatrix} 0 & 0 & 0 & 0 & 0 & 0 & 0 & 0 & 1 & 0 & 0 & 0 \\ 0 & 0 & 0 & 0 & 0 & 0 & 0 & 0 & 0 & 1 & 0 & 0 \\ 0 & 0 & 0 & 0 & 0 & 0 & 0 & 0 & 0 & 0 & 1 & 0 \\ 0 & 0 & 0 & 0 & 0 & 0 & 0 & 0 & 0 & 0 & 0 & 1 \end{bmatrix} \tag{20}$$

During the inverse Fourier transformation, a frequency range of 0.5-20 Hz was considered, which is equivalent to applying a bandpass filter. Trial 4 was chosen as the training set, while Trials 1, 2, 3, 5, and 6 were used as the test set. When selecting the training set, the dataset containing the maximum load was intentionally avoided to ensure that the test set included a maximum load greater than that in the training set and to verify the model's generalization ability to loads outside the training set. The neural network consisted of two LSTM layers and one fully connected layer. The LSTM layers contained 150 neurons with default internal gating mechanisms (tanh and sigmoid). The input time series length l_{sq} was set to 10, meaning that the next load value was predicted using the previous 10 data points. The fully connected layer did not use an additional activation function, and the number of its neurons was also 150. The output layer consisted of a single neuron, which linearly mapped the time-series information to the final load value. The Adam optimizer was used with a learning rate of 0.001, and the loss function was the MSE loss. Training was performed on an NVIDIA GTX 4070 SUPER GPU with a batch size of 64.

(2) Pure data-driven method (DL): This method used LSTM as the main model, with the input being the measured responses and the output being the external excitation. It learned the direct mapping between the responses and the load. The neural network was the same as in the PADL method, and Trial 4 was also selected as the training set.

(3) Pure physical model method (FEM): A 216-DOF finite element model was established based on material properties and geometric dimensions, but model errors were introduced. Specifically, the material density was assumed to be 0.9 times the true value, and the material stiffness 1.2 times the true value. The load was estimated using Eq.(6) and Eq.(8). It should be noted that, in this numerical example, the model errors were deliberately introduced to simulate discrepancies between the finite element model

and the real structure, as well as imperfections in the model tuning process. In the real case study in the next section, the FEM method will be combined with model correction to improve accuracy, ensuring a comparison environment closer to practical applications.

Table 1 lists the natural frequencies of the real model, the simplified model in PADL, and the FEM model, along with their relative errors with respect to the true values. The simplified model in the PADL method shows greater discrepancies from the real case, with an average error of 36% for the first four natural frequencies, while the FEM model has smaller errors, with an average deviation of 15%.

Table 1. Natural frequencies of physical models in different methods and their relative errors with respect to the true values

Modal order	Natural frequency true value (Hz)	PADL		FEM (with model bias)	
		Frequency (Hz)	Error	Frequency (Hz)	Error
1	1.98	1.15	42%	2.28	15%
2	6.29	4.63	26%	7.26	15%
3	11.18	7.25	35%	13.04	16%
4	16.20	9.27	43%	18.70	15%

The R^2 metric was used to quantify the correlation between the estimated loads and the ground truth:

$$R^2 = 1 - \frac{(\boldsymbol{f}_{\text{est}} - \boldsymbol{f}_{\text{true}})^{\text{T}}(\boldsymbol{f}_{\text{est}} - \boldsymbol{f}_{\text{true}})}{(\boldsymbol{f}_{\text{true}} - \bar{\boldsymbol{f}}_{\text{true}})^{\text{T}}(\boldsymbol{f}_{\text{true}} - \bar{\boldsymbol{f}}_{\text{true}})} \tag{21}$$

where $\boldsymbol{f}_{\text{est}}$ represents the estimated load, $\boldsymbol{f}_{\text{true}}$ represents the ground-truth load, and $\bar{\boldsymbol{f}}_{\text{true}}$ represents the average of the true load values. The closer the R^2 value is to 1, the more the predicted results align with the real load.

The loss variations during the training process of the two deep learning methods were recorded and shown in Fig. 6(a). Model performance on the test set was evaluated every 5 epochs, with the results shown in Fig. 6(b). In terms of training loss trends, the PADL method exhibited a faster convergence rate; in contrast, the DL method converged more slowly, with its loss stabilizing after approximately 50 epochs. Regarding test set performance, the PADL method consistently outperformed the DL method throughout the training process, achieving a mean R^2 value close to 1, while the DL method reached a maximum of around 0.9. Additionally, although the training loss of the DL method continued to decrease, its performance on the test set began to decline between epochs 5 to 30. These results demonstrate that the PADL method, by incorporating physical prior information, significantly improves generalization and suppresses overfitting. It also reduces sensitivity of the results to the specific choice of the number of training epochs.

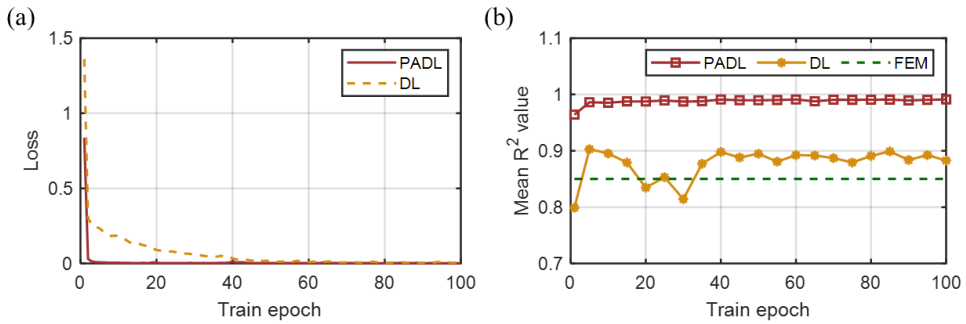

Fig. 6. Training and testing performance comparison of PADL and DL methods: (a) Training loss curves over epochs; (b) Evolution of mean R^2 on the test set.

With the number of training epochs set to 50, a detailed comparison of the R^2 values for the loads estimated by the three methods on the test set is shown in Fig. 7, and the corresponding mean R^2 values are listed in Table 2. The DL method (yellow bars) performed well in Trial 2, Trial 3 and Trial 5, with R^2 values exceeding 0.9. However, when the test loads differed more significantly from those in the training set (Trial 4)—as in Trial 1 and Trial 6—the accuracy of the estimated loads decreased. This is because neural networks generally rely on large amounts of training data to capture the complex behavior patterns. In this case, the limited training data hindered the model's ability to generalize, resulting in a mean R^2 value of only 0.89 in the test set. The FEM method (green bars) performed poorly in Trial 5 and Trial 6, with a mean R^2 of 0.85 on the test set, due to inaccuracies in the physical model parameters.

In contrast, the PADL method (red bars) demonstrated better and more stable performance across all test trials, with a mean R^2 value of 0.99. Compared with the pure data-driven method, the PADL method overcame the limitations associated with small training sample sizes. Compared with the traditional pure physical model method, it reduced dependence on accurate model information. Since it only required a simplified finite element model, it effectively addressed the limitations caused by unknown or inaccurate system parameters.

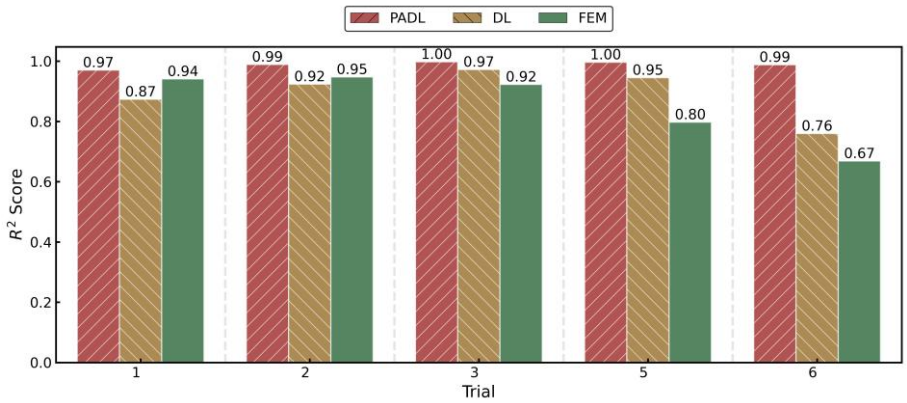

Fig. 7. R^2 values of different methods on the test set

Table 2. Mean R^2 values across all test trials for different identification methods

Method	PADL	DL	FEM
Mean R^2 value	0.99	0.89	0.85

3.2 Unbounded output and temporal scale consistency in PADL

The identified load time histories and error results on the test set are shown in Fig. 8 and Fig. 9. The PADL method demonstrated strong generalization ability on the test set. For example, although the maximum load in the training set was 5.5 N, the model still maintained good prediction performance when faced with test cases beyond this range (e.g., the maximum load in Trial 1 was 9.7 N). This extrapolation capability can be attributed to two key design choices:

(1) Unconstrained output layer: The final output layer was implemented without any activation function (i.e., a plain linear layer), rather than using bounded functions like Sigmoid or Tanh. This design avoids restricting the predicted values to the range of the training data and, in theory, allows the model to produce outputs of arbitrary magnitude.

(2) Scale-consistent temporal modeling: Although the proposed PADL framework includes nonlinear components (LSTM layers), it was trained on inputs that were normalized with respect to the maximum load in the entire training set. This normalization, combined with the model's ability to learn temporal dependencies, enabled consistent scaling between inputs and outputs. Consequently, even when test inputs were outside the training range, the model preserved proportional mapping patterns and demonstrated robust extrapolation performance.

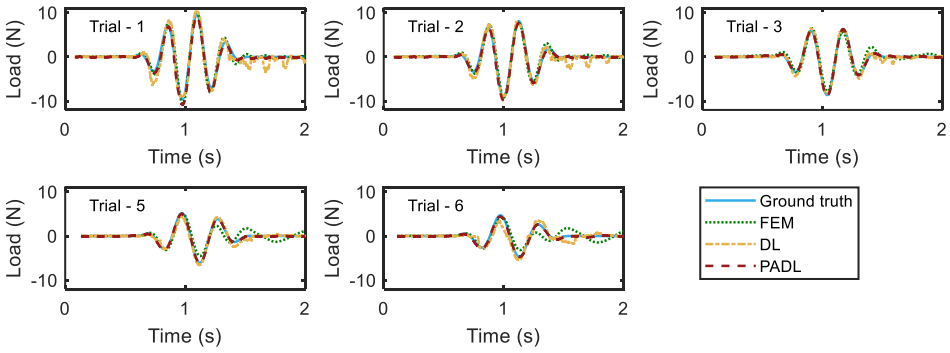

Fig. 8. Load identification time histories of different methods on the test set

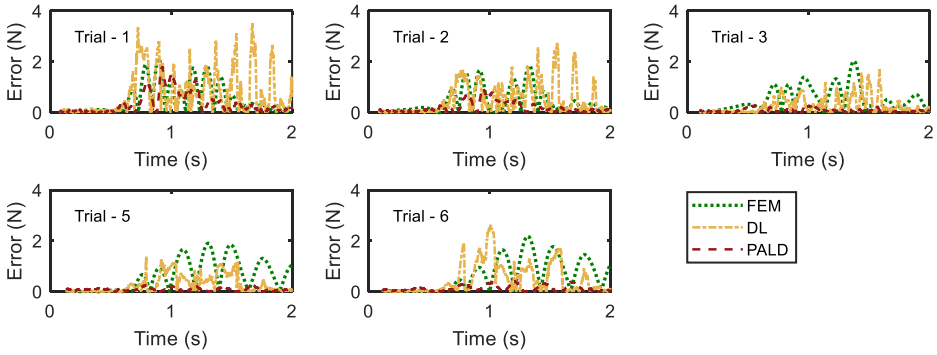

Fig. 9. Absolute load identification errors of different methods on the test set

3.3 Effect of extended states

The importance of the state extension mechanism for prediction accuracy is demonstrated in Fig. 10 by comparing the performance of the full PADL method (which, in addition to the measured response $\boldsymbol{y}$, uses both the estimated unobserved states $\tilde{\boldsymbol{z}}$ and the load $\tilde{\boldsymbol{f}}$ as inputs) with that of its variant PADL-f (which uses the measured response $\boldsymbol{y}$ and only the estimated load $\tilde{\boldsymbol{f}}$ as inputs). The results show that PADL-f, which lacks the extended states $\tilde{\boldsymbol{z}}$, exhibits a noticeable drop in overall accuracy compared to the full-input PADL method. This performance gap stems from the loss of physical information completeness: the extended states $\tilde{\boldsymbol{z}}$ not only capture the responses of unmeasured DOFs but also embed multi-dimensional state coupling among displacement, velocity, and acceleration. These states provide implicit structural dynamic constraints to the neural network and enhance its ability to learn and maintain physical consistency between load and response. This finding supports the core idea behind PADL: incorporating multi-level physical information improves generalization performance.

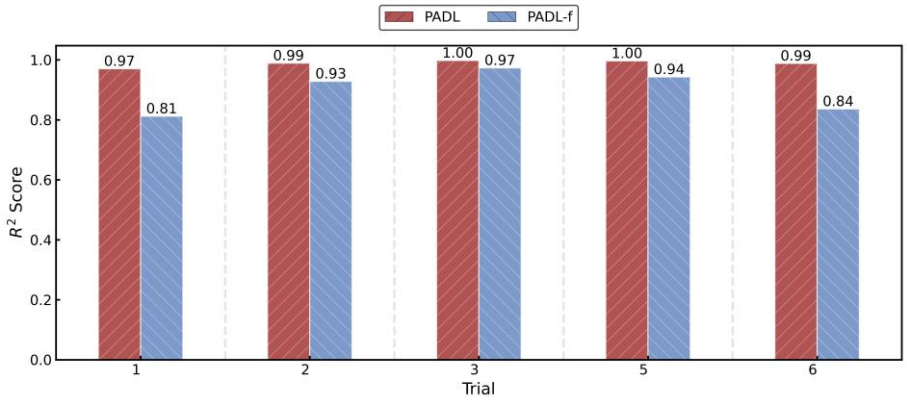

Fig. 10. R^2 values of load identification by PADL and PADL-f

4. Laboratory test

This section investigates the effectiveness of the proposed PADL framework in handling different types of loads through laboratory experiments on a four-story shear frame, including random and impulsive load scenarios.

4.1 Test equipment and setup

In the laboratory tests, a four-story, single- span shear frame made of steel and hard plastic was used. The story height and span were both 0.4 m. To increase structural complexity, elastic ropes were used to constrain the frame, as shown in Fig. 11. The theoretical material properties were as follows: the columns had an elastic modulus of 2.1×10^{11} Pa, a density of 7.9×10^{3} kg/m³, a section height of 0.03 m, and a section width of 0.15 m. The beams had an elastic modulus of 2.32×10^{9} Pa, a density of 1.625×10^{3} kg/m³, a section height of 0.002 m, and a section width of 0.15 m. Acceleration sensors

were installed on all four stories of the frame to capture lateral vibration acceleration. A load sensor (PCB 288D01), capable of simultaneously measuring both force and acceleration, was installed on the second story. All testing equipment and their corresponding models are shown in Fig. 11.

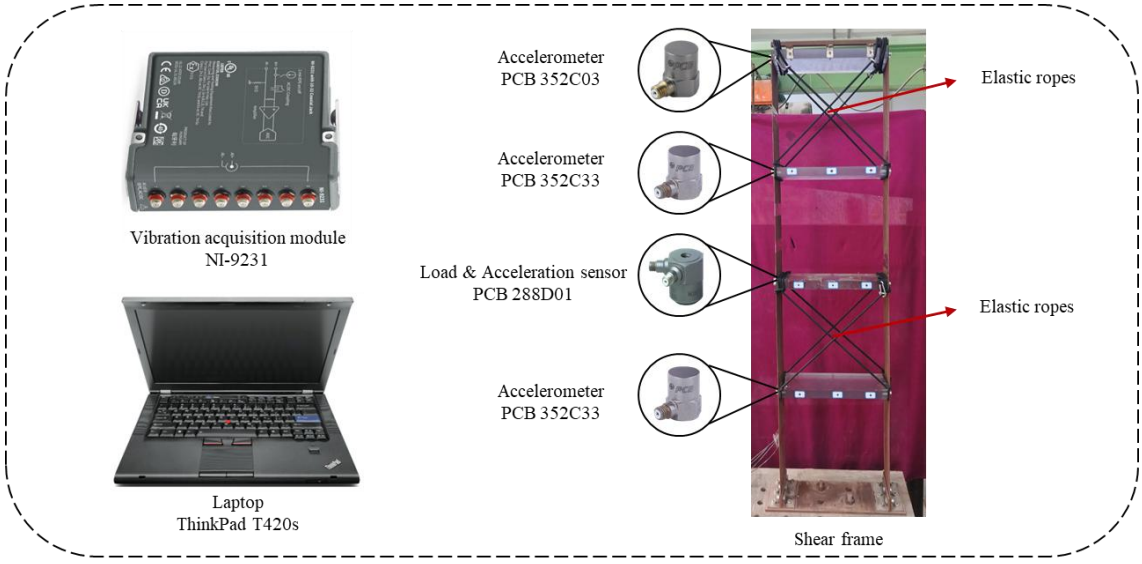

Fig. 11. Shear frame structure and test equipment

4.2 Random load identification

Random lateral loads were applied to the second floor of the structure in nine separate trials. Both load and acceleration data were collected at a sampling frequency of 1000 Hz. Each trial was indexed according to the peak amplitude of the applied load. The maximum load amplitudes are shown in **Błąd! Nie można odnaleźć źródła odwołania.**(a), and the time-domain statistics of several trials are presented in **Błąd! Nie można odnaleźć źródła odwołania.**(b). The time history and frequency spectrum of the applied load in the first trial are shown in **Błąd! Nie można odnaleźć źródła odwołania.**.

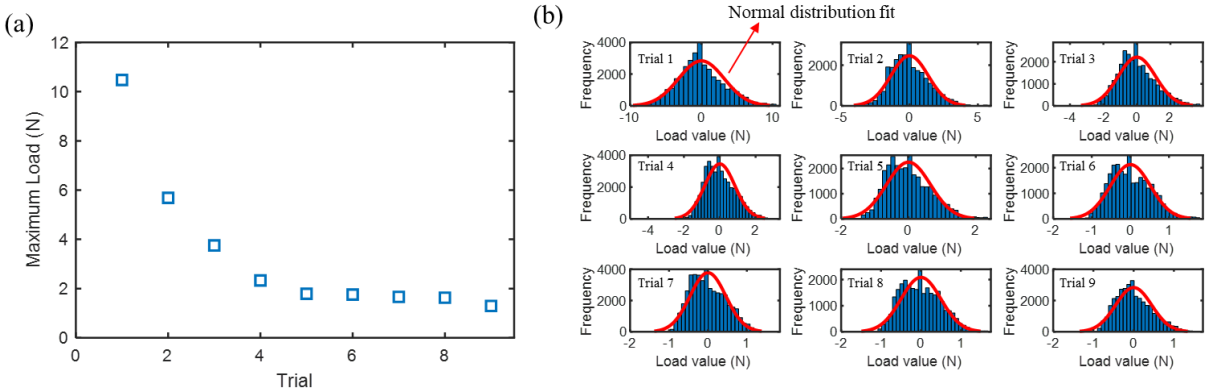

Fig. 12. Overview of the random load dataset: (a) trial ID and maximum load amplitude; (b) time-domain statistical analysis of the load

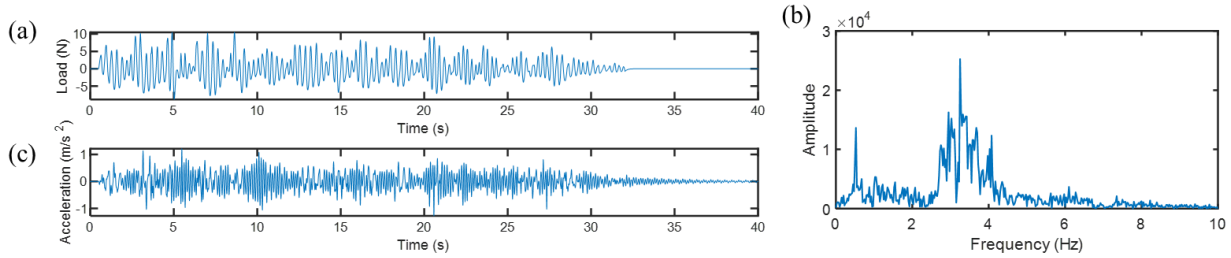

Fig. 13. Load and response in Trial 1: (a) load time history; (b) load spectrum; (c) acceleration response time history as measured by the first-floor sensor

Load identification was carried out using the following three methods:

(1) PADL: A simplified four-degree-of-freedom model was used as prior knowledge, as shown in Fig. 5(a), where the mass and stiffness parameters were arbitrarily assumed as $m_1 = m_2 = m_3 = m_4 = 3$ kg and $k_1 = k_2 = k_3 = k_4 = 10000$ N/m. The mass and stiffness matrices $\boldsymbol{M}$ and $\boldsymbol{K}$ were constructed according to Eq.(18) and Eq.(19). The Rayleigh damping coefficients α and β were both set to 0.01. During the inverse Fourier transform, only the frequency range from 1 Hz to 7 Hz was considered. The neural network architecture was the same as that described in Section 3.2. Trials 2, 4, 6, and 8 were used as the training set, while Trials 1, 3, 5, 7, and 9 were used as the test set.

(2) DL: The purely data-driven method employed the same neural network architecture and training conditions as the PADL method.

(3) FEM: In the purely physics-based method, the accuracy of the model significantly affects the performance of load identification, and therefore model calibration is required. A two-dimensional finite element model with 60-DOF was constructed based on the material properties and geometric dimensions. Inter-story stiffness and mass parameters were calibrated using the identified natural frequencies and mode shapes extracted from the structure's impulse response, following the procedure in [34]. The measured natural frequencies of the frame and those of the calibrated model are listed in Table 3. The damping ratios of the first two modes were both identified as 0.06. Using the identified frequencies and damping ratios, a Rayleigh damping matrix was constructed. Load identification was then performed using Eq.(6) and Eq.(8).

Table 3 Identified and calibrated natural frequencies of the structure

Modal order	Natural frequency (Hz)		Relative error
	Test	FEM	
1	2.36	2.38	0.7%
2	7.06	7.00	-0.8%
3	12.12	12.04	-0.6%
4	14.93	15.04	0.7%

The variations in training loss and test set R^2 with increasing training epochs are shown in Fig. 14. The PADL method consistently outperformed both the DL and FEM methods and demonstrated more stable performance as the number of training epochs increased.

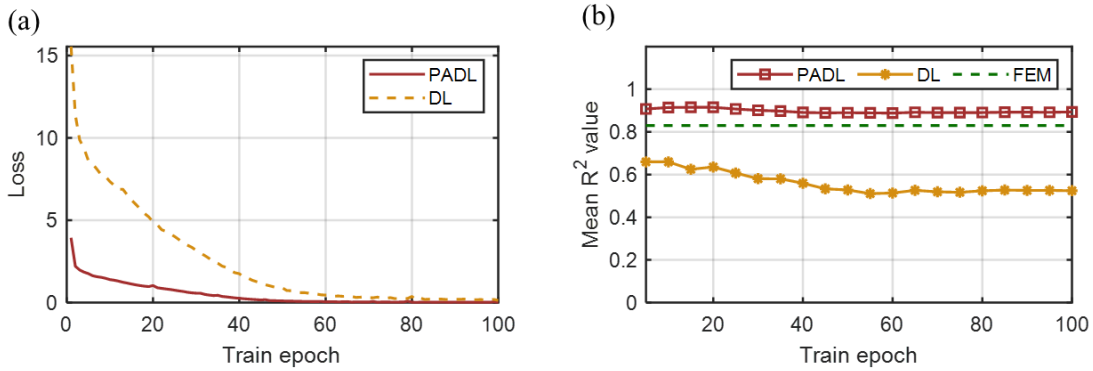

Fig. 14. Training and testing performance of different methods in random load identification: (a) training loss curves over epochs; (b) evolution of mean R^2 on the test set

With the number of training epochs set to 10, Fig. 15 shows the R^2 values for random load identification across the test trials using the three methods, and Table 4 lists the corresponding mean values. The purely physics-based method exhibited limited accuracy due to model errors, with a mean R^2 value of 0.82. The purely data-driven method performed worse, achieving a mean R^2 of only 0.66, as the limited training data made it difficult to effectively capture the high-dimensional mapping between measured responses and external loads.

In contrast, the PADL method achieved consistently high accuracy, with R^2 values exceeding 0.89 across all test cases. As an example, the predicted load curve for Trial 1 and the corresponding error are shown in Fig. 16. The time-history error of the PADL prediction is significantly lower than that of the other two methods. Although the simplified physical model provides only limited information, it still serves as a channel for injecting physical knowledge into the neural network. This confirms that the proposed method effectively guides the learning process by embedding physics-informed knowledge and achieves a synergistic integration of physical principles and data-driven features.

In addition, the maximum load in the training set was only 6 N (from Trial 2), while the test set included a larger load of up to 11 N (at 5 s in Trial 1). The neural network design in the PADL method was still able to extrapolate beyond the training range. This is because the fully connected output layer did not use bounded activation functions such as Sigmoid or Tanh, but instead produced linear outputs. As a result, the model's prediction range was not restricted by the maximum value in the training data.

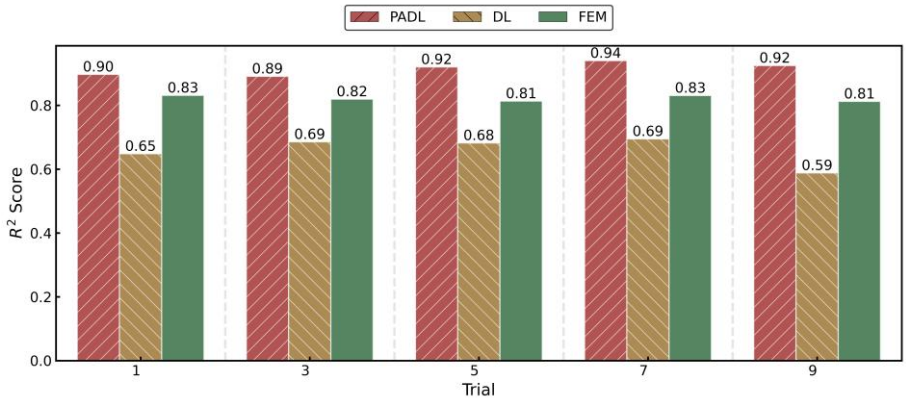

Fig. 15. R^2 of the identified random loads in the test set using different methods

Table 4 Mean R^2 values across all test trials for different identification methods

Method	PADL	DL	FEM
Mean R^2 value	0.91	0.66	0.82

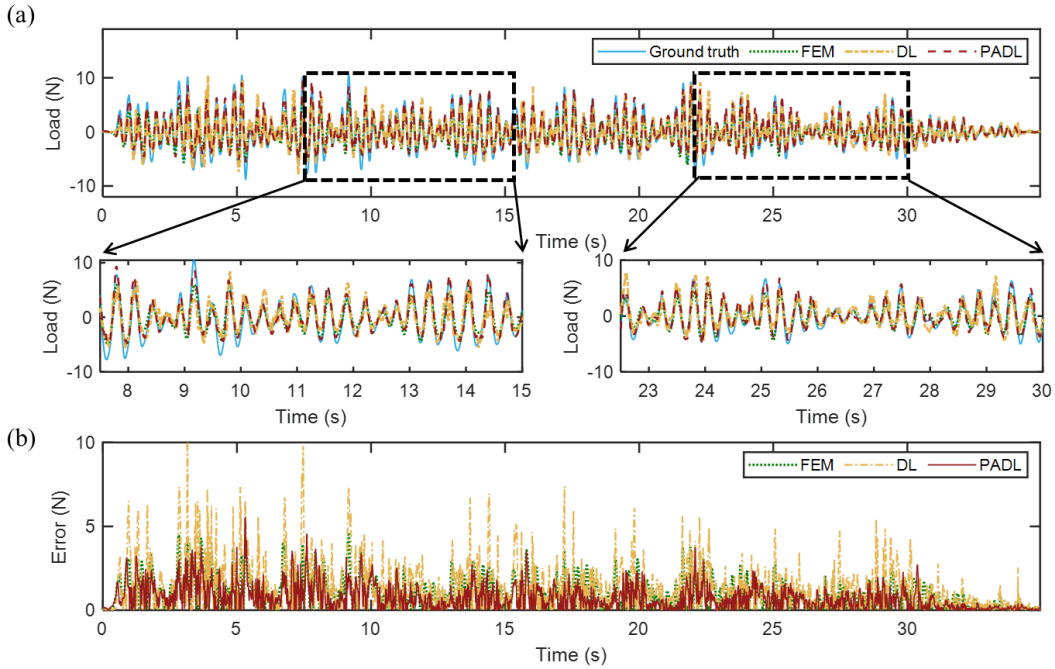

Fig. 16. Random load identification results for Trial 1: (a) load time history curve; (b) absolute errors of the identified loads

4.3 Impulse load identification

This section evaluates the performance of the proposed method in identifying impulse loads. Impulse excitation was applied to the second story of the frame by hammering, and both the load and acceleration responses from all four stories were recorded at a sampling frequency of 5000 Hz. The collected data were sorted in descending order based on the peak load amplitude, as shown in Fig. 17(a). As an example, Fig. 17(b) shows the time histories of the applied load and the 1st-floor acceleration response in Trial 1, while the corresponding load spectrum is presented in Fig. 17(c).

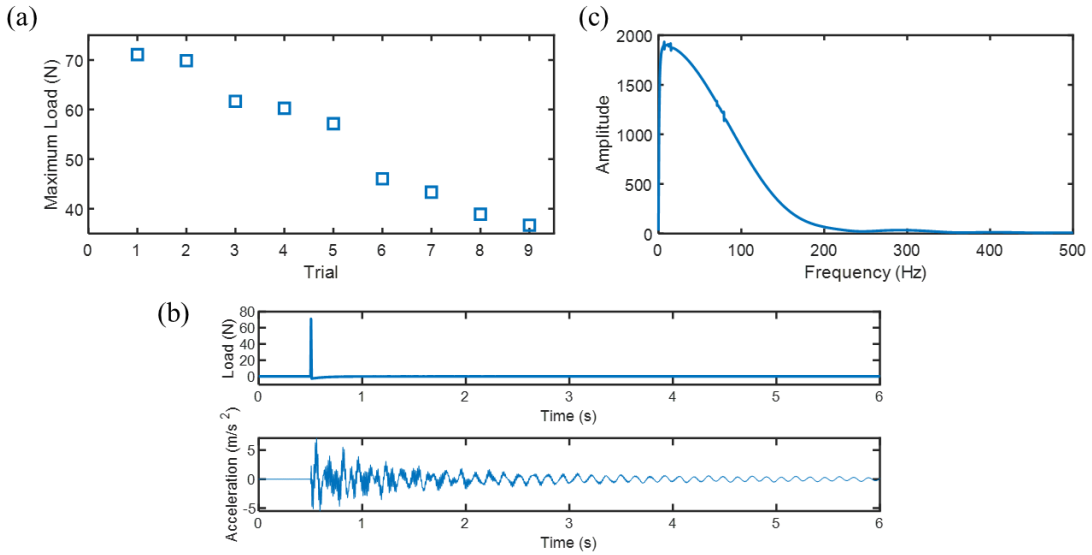

Fig. 17. Overview of the impulse load dataset: (a) peak values of the impulse loads; (b) load time history and 1st-floor acceleration in Trial 1; (c) load spectrum in Trial 1

Fig. 18(a) shows the load spectrum obtained using the FEM-based FRF method, which exhibits numerous singularities. To investigate the effect of the frequency range on the identification results, the lower bound of the frequency domain was fixed at 1 Hz, while the upper bound was varied among 50, 100, 150, and 200 Hz. The corresponding time-domain load signals obtained through inverse Fourier transform are shown in Fig. 18(b). All of these results significantly deviate from the ground truth. This discrepancy arises because the ideal impulse load has an infinite bandwidth with a constant amplitude across all frequencies. Although the actual impulse spectrum decays with frequency, it still spans a very wide frequency band. When a narrow frequency range is selected, the truncated spectrum corresponds to a convolution of the original impulse with a rectangular window function in the time domain. This leads to an attenuated peak amplitude and non-physical oscillations (Gibbs phenomenon) on both sides of the pulse, as seen in the "50 Hz" curve in Fig. 18(b). Moreover, when higher frequency bands are used, experimental noise and modeling errors are amplified in the inverse process, resulting in severe oscillations in the time-domain signal, as observed in the "100 Hz," "150 Hz," and "200 Hz" curves in Fig. 18(b).

Therefore, the frequency-domain method is not ideal for impulse load identification. Nevertheless, it still provides a form of physical guidance that can be integrated into the PADL framework. The following section evaluates the performance of the proposed method in identifying impulse loads.

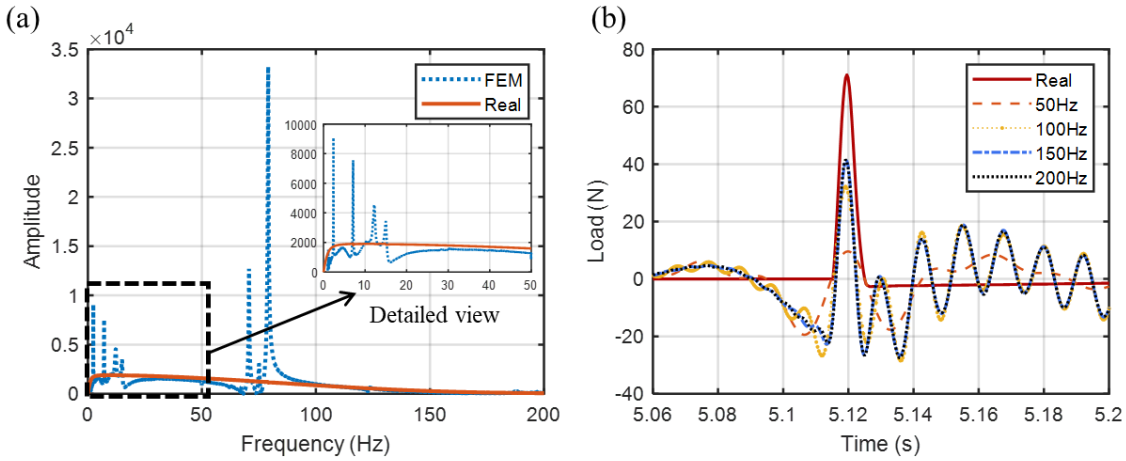

Fig. 18. Ill-posedness in direct frequency-domain inversion: (a) load spectrum; (b) time-domain impulse responses obtained by inverse Fourier transform over different frequency ranges

Trials 2, 4, 6, and 8 were used as the training set, while Trials 1, 3, 5, 7, and 9 were used as the test set. The PADL method used the same simplified 4-DOF model as in previous sections. Its physical priors and state extension strategy were consistent with those applied in the physics-based approach, while the neural network configuration remained unchanged from Section 4.2. To generate the extended states, the inverse Fourier transform was applied within a frequency range of 1–50 Hz. The purely data-driven method shared the same conditions as the PADL method.

The training loss and test results are shown in Fig. 19. PADL consistently demonstrated better performance, achieving R^2 scores close to 1 and exhibiting stable generalization on the test set as training progressed. In contrast, the traditional DL method yielded lower R^2 scores across all training epochs. Moreover, the test performance of DL fluctuated with the number of training epochs, revealing its sensitivity to training duration and instability in learning. This indicates that careful selection of the training epoch is required when using purely data-driven approaches.

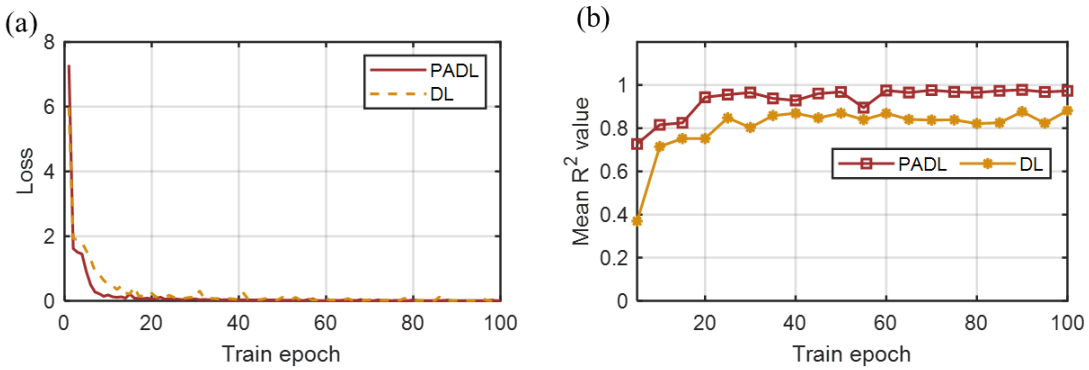

Fig. 19. Training and testing performance of different methods in impulse load identification: (a) training loss curves over epochs; (b) evolution of mean R^2 on the test set

With the number of training epochs set to 60, the R^2 values for load identification on the test set using the PADL and DL methods are shown in Fig. 20, and the corresponding mean values are listed in Table 5. The identified load time histories and the corresponding errors are presented in Fig. 21.

The traditional DL method yielded lower R^2 scores than PADL and performed poorly in Trials 1 and 3, with significant discrepancies between the identified loads and the ground truth. In contrast, the PADL method achieved higher R^2 values and exhibited more consistent performance across all test trials. This improvement can be attributed to the integration of physical knowledge, which allows PADL to outperform purely data-driven methods in terms of identification accuracy.

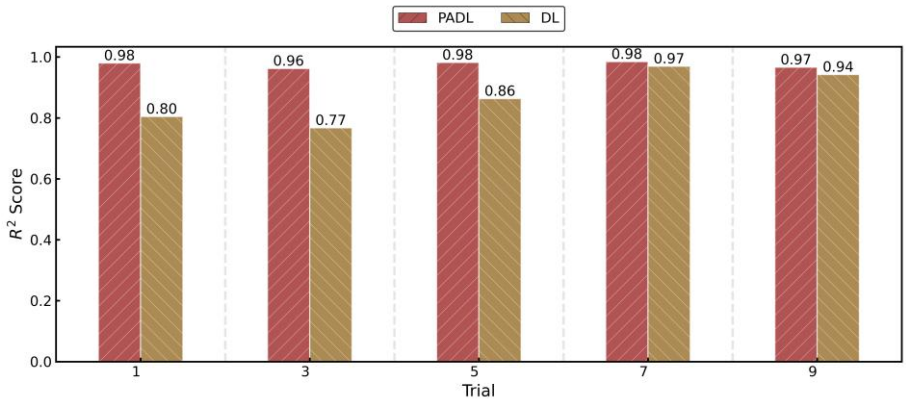

Fig. 20. R^2 of identified impulse loads in the test set using different methods

Table 5 Mean R^2 values across all test trials for different identification methods

Method	PADL	DL
Mean R^2	0.97	0.87

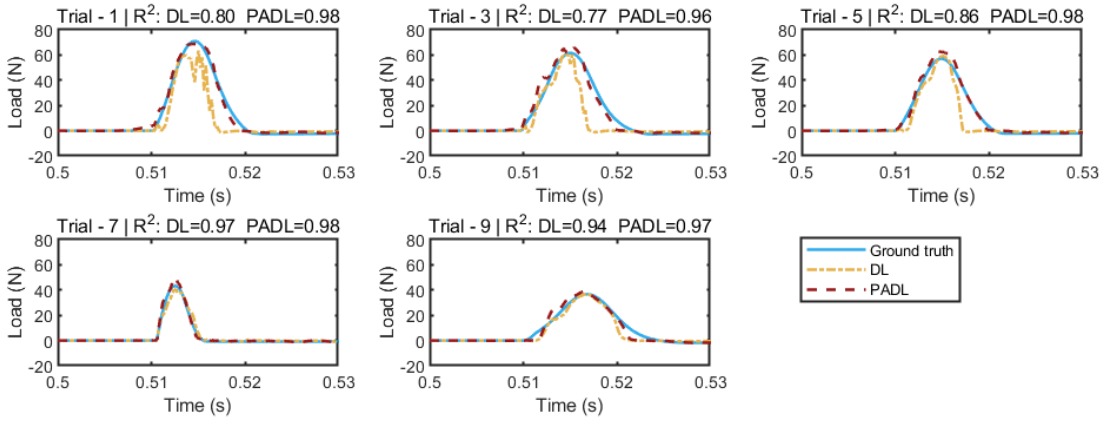

Fig. 21. Time-domain identification results of the impulse load

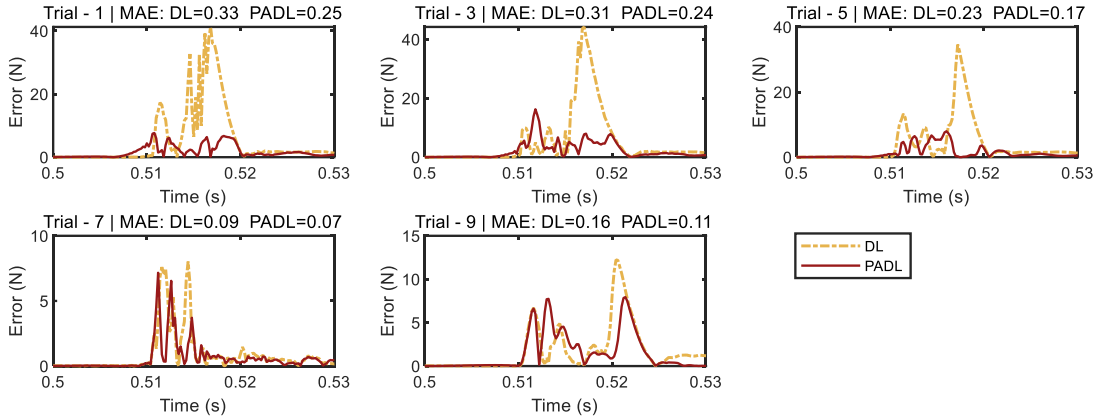

Fig. 22. Absolute error in the impulse load identification

5. Conclusion

This study introduces a novel method, PADL, for structural dynamic load identification. The core idea lies in obtaining a rough estimation of the external loads and full-state responses using a simplified physical model, followed by a lightweight neural network that compensates for modeling errors through data-driven learning. Both numerical simulations and laboratory experiments were conducted to demonstrate the advantages of the proposed method over conventional purely physics-based and purely data-driven approaches. The main conclusions are as follows:

(1) PADL adopts a hybrid modeling strategy that integrates simplified physical modeling, full-state estimation, and data-based residual compensation. Compared with purely data-driven methods that rely solely on the mapping between measured responses and external loads, PADL significantly reduces the reliance on labeled data and achieves higher load identification accuracy. It demonstrates superior prediction accuracy even with a small training dataset and converges faster within fewer training epochs. This highlights its potential for applications in data-scarce and resource-constrained scenarios. Moreover, in contrast to conventional purely physics-based models, PADL shows lower sensitivity to the accuracy of physical parameters and does not require complex model calibration, which offers greater practicality and robustness.

(2) The core of the PADL framework is the expansion of the feature space using structural dynamics principles to provide physically constrained input features for the neural network. The FRF-based full-state estimation avoids reliance on specific types of measured responses by reconstructing pseudo-measurements of unobserved DOFs through a generalized inverse approach, which reduces the complexity of the learning task. Although frequency truncation limits the FRF method's ability to reconstruct the time history of impulse loads, the resulting estimates still retain essential physical characteristics. These estimates can be embedded into the neural network as physically-informed priors, effectively guiding the identification and improving performance for impulse loads.

(3) Unlike conventional neural network designs that employ activation functions to constrain the output range, PADL uses a linear mapping in the output layer, which removes the bounded output constraint. This design enables the predicted load values to exceed the amplitude range seen in the training data. Both simulation and experimental results demonstrate that this unbounded output design enhances the model's extrapolation capability for extreme loads and improves its generalization performance.

It should be noted that the proposed method still falls within the scope of supervised learning, where the training process relies on access to ground-truth load data. However, in practical engineering applications, external loads are often difficult to measure directly. Therefore, future research will explore hybrid modeling approaches based on unsupervised or semi-supervised learning to reduce dependency on labeled load data. In addition, this study focused primarily on validating the effectiveness of the hybrid modeling framework, without conducting a systematic investigation into the neural network architecture or hyperparameter selection. Further research is needed to address these optimization issues in depth.

Declaration of Competing Interest

The authors declare that they have no known competing financial interests or personal relationships that could have appeared to influence the work reported in this paper.

Declaration of Generative AI technologies in the writing process

During the preparation of this work the authors used Google Translate and ChatGPT to correct the grammar and punctuation of the text. After using these tools, the authors reviewed and edited the content as needed and take full responsibility for the content of publication.

Acknowledgements

The authors gratefully acknowledge the support of the National Key Research and Development Program of China (2024YFF0507103), the National Natural Science Foundation of China (NSFC) (52378285), the Liaoning Provincial Natural Science Foundation of China (2024-MS-020) and the National Science Centre of Poland (2020/39/B/ST8/02615).

References

[1] J. Liu, X. Meng, D. Zhang, C. Jiang, X. Han, An efficient method to reduce ill-posedness for structural dynamic load identification, Mechanical Systems and Signal Processing 95 (2017) 273–285. https://doi.org/10.1016/j.ymssp.2017.03.039.

[2] K. Mendrok, Z. Dworakowski, A review of methods for excitation force reconstruction, Diagnostyka 20 (2019) 11–19. https://doi.org/10.29354/diag/110241.

[3] R. Liu, E. Dobriban, Z. Hou, K. Qian, Dynamic Load Identification for Mechanical Systems: A Review, Arch Computat Methods Eng 29 (2022) 831–863. https://doi.org/10.1007/s11831-021-09594-7.

[4] M. Acosta, S. Kanarachos, Tire lateral force estimation and grip potential identification using Neural Networks, Extended Kalman Filter, and Recursive Least Squares, Neural Comput & Applic 30 (2018) 3445–3465. https://doi.org/10.1007/s00521-017-2932-9.

[5] X. Zhang, W. He, Q. Cui, T. Bai, B. Li, J. Li, X. Li, WavLoadNet: Dynamic Load Identification for Aeronautical Structures Based on Convolution Neural Network and Wavelet Transform, Applied Sciences 14 (2024) 1928. https://doi.org/10.3390/app14051928.

[6] L. Wang, Han ,Xu, Liu ,Jie, He ,Xiaoqiao, F. and Huang, A new regularization method and application to dynamic load identification problems, Inverse Problems in Science and Engineering 19 (2011) 765–776. https://doi.org/10.1080/17415977.2010.531468.

[7] L. Caglio, A. Sadeqi, H. Stang, E. Katsanos, Joint input-state estimation of structures subjected to complex loads via augmented Kalman Filter with physics informed latent force models, Mechanical Systems and Signal Processing 223 (2025) 111852. https://doi.org/10.1016/j.ymssp.2024.111852.

[8] Y. Li, Y. Luo, H.-P. Wan, C.-B. Yun, Y. Shen, Identification of earthquake ground motion based on limited acceleration measurements of structure using Kalman filtering technique, Structural Control and Health Monitoring 27 (2020) e2464. https://doi.org/10.1002/stc.2464.

[9] J. Jiang, S. Luo, M.S. Mohamed, Z. Liang, Real-Time Identification of Dynamic Loads Using Inverse Solution and Kalman Filter, Applied Sciences 10 (2020) 6767. https://doi.org/10.3390/app10196767.

[10] D.-C. Lin, Adaptive weighting input estimation for nonlinear systems, International Journal of Systems Science 43 (2012) 31–40. https://doi.org/10.1080/00207721003764141.

[11] L.N. Guo, Y. Ding, Z. Wang, G.S. Xu, B. Wu, A dynamic load estimation method for nonlinear structures with unscented Kalman filter, Mechanical Systems and Signal Processing 101 (2018) 254–273. https://doi.org/10.1016/j.ymssp.2017.07.047.

[12] A. Kazemi Amiri, C. Bucher, A procedure for in situ wind load reconstruction from structural response only based on field testing data, Journal of Wind Engineering and Industrial Aerodynamics 167 (2017) 75–86. https://doi.org/10.1016/j.jweia.2017.04.009.

[13] H.M. Alqam, A.K. Dhingra, Frequency Response-Based Indirect Load Identification Using Optimum Placement of Strain Gages and Accelerometers, Journal of Vibration and Acoustics 141 (2019). https://doi.org/10.1115/1.4042709.

[14] Y. Jia, Z. Yang, Q. Song, Experimental study of random dynamic loads identification based on weighted regularization method, Journal of Sound and Vibration 342 (2015) 113–123. https://doi.org/10.1016/j.jsv.2014.12.010.

[15] D. Fu, L. Wang, G. Lv, Z. Shen, H. Zhu, W.D. Zhu, Advances in dynamic load identification based on data-driven techniques, Engineering Applications of Artificial Intelligence 126 (2023) 106871. https://doi.org/10.1016/j.engappai.2023.106871.

[16] H. Yang, J. Jiang, G. Chen, J. Zhao, Dynamic load identification based on deep convolution neural network, Mechanical Systems and Signal Processing 185 (2023) 109757. https://doi.org/10.1016/j.ymssp.2022.109757.

[17] W. He, X. Zhang, Z. Feng, Q. Leng, B. Xu, X. Li, Random Dynamic Load Identification with Noise for Aircraft via Attention Based 1D-CNN, Aerospace 10 (2023) 16. https://doi.org/10.3390/aerospace10010016.

[18] W. He, B. Li, Z. Feng, X. Zhang, H. Sun, Dynamic Load Identification at Natural Frequencies for Aircraft via Attention Based 1D-CNN, J. Phys.: Conf. Ser. 2762 (2024) 012030. https://doi.org/10.1088/1742-6596/2762/1/012030.

[19] H. Yang, J. Jiang, G. Chen, M.S. Mohamed, F. Lu, A Recurrent Neural Network-Based Method for Dynamic Load Identification of Beam Structures, Materials 14 (2021) 7846. https://doi.org/10.3390/ma14247846.

[20] S. Hochreiter, J. Schmidhuber, Long Short-Term Memory, Neural Computation 9 (1997) 1735–1780. https://doi.org/10.1162/neco.1997.9.8.1735.

[21] J. Zhou, L. Dong, W. Guan, J. Yan, Impact load identification of nonlinear structures using deep Recurrent Neural Network, Mechanical Systems and Signal Processing 133 (2019) 106292. https://doi.org/10.1016/j.ymssp.2019.106292.

[22] J. Chung, C. Gulcehre, K. Cho, Y. Bengio, Empirical Evaluation of Gated Recurrent Neural Networks on Sequence Modeling, (2014). https://doi.org/10.48550/arXiv.1412.3555.

[23] M. Impraimakis, Deep recurrent-convolutional neural network learning and physics Kalman filtering comparison in dynamic load identification, Structural Health Monitoring 24 (2025) 1752–1782. https://doi.org/10.1177/14759217241262972.

[24] T. Feng, A. Duan, L. Guo, H. Gao, T. Chen, Y. Yu, Deep learning based load and position identification of complex structure, in: 2021 IEEE 16th Conference on Industrial Electronics and Applications (ICIEA), 2021: pp. 1358–1363. https://doi.org/10.1109/ICIEA51954.2021.9516129.

[25] M. Raissi, P. Perdikaris, G.E. Karniadakis, Physics-informed neural networks: A deep learning framework for solving forward and inverse problems involving nonlinear partial differential equations, Journal of Computational Physics 378 (2019) 686–707. https://doi.org/10.1016/j.jcp.2018.10.045.

[26] Y. Hu, H.-H. Tsang, N. Lam, E. Lumantarna, Physics-informed neural networks for enhancing structural seismic response prediction with pseudo-labelling, Archiv.Civ.Mech.Eng 24 (2023) 7. https://doi.org/10.1007/s43452-023-00820-6.

[27] S. Moradi, B. Duran, S. Eftekhar Azam, M. Mofid, Novel Physics-Informed Artificial Neural Network Architectures for System and Input Identification of Structural Dynamics PDEs, Buildings 13 (2023) 650. https://doi.org/10.3390/buildings13030650.

[28] J. Zhou, Y. Cai, L. Dong, B. Zhang, Z. Peng, Data-physics hybrid-driven deep learning method for impact force identification, Mechanical Systems and Signal Processing 211 (2024) 111238. https://doi.org/10.1016/j.ymssp.2024.111238.

[29] J. Liu, Y. Li, L. Sun, Y. Wang, L. Luo, Physics and data hybrid-driven interpretable deep learning for moving force identification, Engineering Structures 329 (2025) 119801. https://doi.org/10.1016/j.engstruct.2025.119801.

[30] Y. Yin, V. Le Guen, J. Dona, E. de Bézenac, I. Ayed, N. Thome, P. Gallinari, Augmenting physical models with deep networks for complex dynamics forecasting*, J. Stat. Mech. 2021 (2021) 124012. https://doi.org/10.1088/1742-5468/ac3ae5.

[31] Y. Ji, Y. Huang, J. Zeng, L. Ren, Y. Chen, A physical–data-driven combined strategy for load identification of tire type rail transit vehicle, Reliability Engineering & System Safety 253 (2025) 110493. https://doi.org/10.1016/j.ress.2024.110493.

[32] Y. He, J.P. Yang, Using Kalman filter to estimate the pavement profile of a bridge from a passing vehicle considering their interaction, Acta Mech 232 (2021) 4347–4362. https://doi.org/10.1007/s00707-021-03055-9.

[33] X. Hu, Q. Zeng, Z. Duan, C. Liu, J. Lin, Q. Fan, Z. Zhang, Estimation of Road Roughness Based on Both the Sprung and Unsprung Response of a Moving Vehicle Over Ordinary Roads: Modeling, Experiments and Discussions, Int. J. Str. Stab. Dyn. 24 (2024) 2450115. https://doi.org/10.1142/S0219455424501153.

[34] X. An, J. Hou, D. Xu, G. Dong, Computer vision-based substructure isolation method for localized damage identification, Structures 70 (2024) 107660. https://doi.org/10.1016/j.istruc.2024.107660.